

LONG WAVELENGTH ASTROPHYSICS

by

Liam Dean Connor

A thesis submitted in conformity with the requirements
for the degree of Doctor of Philosophy
Graduate Department of Astronomy and Astrophysics
University of Toronto

© Copyright 2016 by Liam Dean Connor

—

Contents

1	Introduction	1
1.1	Digital telescopes	2
1.2	The time-domain sky	4
1.2.1	Propagation effects	5
1.3	Fast Radio Bursts	9
1.3.1	Models	12
1.3.2	Empirical constraints	16
1.4	Thesis Outline	18
2	The Canadian Hydrogen Intensity Mapping Experiment	21
2.1	Chapter Overview	21
2.2	Introduction	22
2.3	CHIME Science	23
2.3.1	21 cm Cosmology	23
2.3.2	CHIME-pulsar	27
2.3.3	CHIME-FRB	28
2.4	Instrument	29
2.4.1	Clover-feeds	30
2.4.2	Amplifiers	31
2.4.3	Correlator	31

2.4.4	Beams	32
2.5	Conclusion	34
	Bibliography	40

List of Tables

2.1	CHIME Parameters	30
-----	----------------------------	----

Chapter 1

Introduction

The most interesting advances in science come not from concerted efforts to answer specific questions, but rather from exploring a new volume of parameter space. The father of observational astronomy, Galileo, did not construct Lippershey’s telescope in order to discover the Jovian satellites. Instead, he used a novel tool to investigate supra-human magnitudes and spatial resolution to observe three moons “totally invisible by their smallness” orbiting Jupiter (Drake, 1978).

The tradition has continued in the centuries since, particularly in astrophysics where we humans have little innate intuition (by definition everything we study is outside of this world). Pulsars, for example, were discovered accidentally with a radio telescope that was built to study interstellar scintillation in quasars (Hewish et al., 1968). The whole field commenced because graduate student Jocelyn Bell noticed extra “scruff” on her chart recorder. Dark matter and dark energy are two more examples of largely unpredicted, but revolutionary, discoveries (Zwicky, 1933; Riess et al., 1998; Perlmutter et al., 1999). A more recently uncovered phenomenon is the fast radio burst (FRB), a primary focus of this thesis. FRBs were discovered as a result of searching new regions of dispersion measure space at high time resolution.

The tools that are now used to explore the long-wavelength sky have been expanded

vastly in scope in the last decade. The unprecedented speed and sensitivity that Moore’s law has afforded twenty-first century radio telescopes has given us access to previously veiled physics.

1.1 Digital telescopes

A telescope’s primary purpose is to provide for us spatial, temporal, and chromatic information about electromagnetic fields on the sky. Mathematically, telescopes first perform a spatial Fourier transform of the incoming waveform (from \mathbf{x} - to \mathbf{k} -modes), traditionally with a mirror or reflector, and then another Fourier transform in time (from τ to ν) to separate the signal by wavelength, with, e.g., a diffraction grating. The electromagnetic wave’s modulus is typically then effectively squared. This destroys phase information, whether a bolometer or a charge-coupled device (CCD) is used. Modern radio telescopes carry out a similar set of steps, except at some stages they use powerful computers in place analog instrumentation. For example, channelization can be done in software rather than with diffraction. They also have the ability to preserve phase information by measuring a quantity proportional to the electric field, namely voltage.

In an era when electric fields can effectively be sampled billions of times per second, radio telescopes are becoming almost entirely digital. While the cost of constructing large single-dish telescopes is not expected to decrease substantially, the cost of building large computing clusters is, which makes it economically and strategically sensible to point one’s telescope and to channelize in software. This fact has ushered in a new era of broad-band, wide-field interferometers with large numbers of feeds. These include the Precision Array for Probing the Epoch of Reionization (PAPER), the Murchison Widefield Array (MWA), and the Low-Frequency Array (LOFAR) (Tingay et al., 2013; Parsons et al., 2014; van Haarlem et al., 2013). The Canadian Hydrogen Intensity Mapping Experiment (CHIME), which is central to this thesis, is another principally digital telescope.

Radio interferometry was first developed in the 1940s when Ryle and Vonberg constructed a dipole array at 175 MHz (Thompson et al., 1986). Based on the Michelson interferometer, it was realized that the same spatial resolution of a large dish with diameter, D , could be achieved by correlating two antennas separated by D . In a classical interferometer, the quantity we measure is called a “visibility”, denoted in this text as $V_{m,n}$. It is the time-averaged correlation of the signals x_m and x_n .

$$V_{m,n} = \langle x_m x_n^* \rangle. \quad (1.1)$$

This can be written as an integral over all directions, $\hat{\mathbf{k}}$, on the sky, weighted by the complex gains, $g(\hat{\mathbf{k}})$, in that direction.

$$V_{m,n} = \int d^2\hat{\mathbf{k}} g_m(\hat{\mathbf{k}}) g_n^*(\hat{\mathbf{k}}) T(\hat{\mathbf{k}}) e^{2\pi i \hat{\mathbf{k}} \cdot \mathbf{d}_{m,n}} \quad (1.2)$$

Here the baseline vector between antennas m and n is given by $\mathbf{d}_{m,n}$, and $T(\hat{\mathbf{k}})$ is the sky brightness temperature in the direction $\hat{\mathbf{k}}$. This is not a thermodynamic temperature, but the temperature given by the Rayleigh-Jeans law,

$$T = \frac{c^2 I_\nu}{2\nu^2 k_b}, \quad (1.3)$$

where I_ν is specific intensity and k_b is Boltzmann’s constant.

For an N -element array, there are $N(N+1)/2$ unique baselines that must be computed, i.e. for each frequency and at each time, Eq. 1.1 must be calculated $N(N+1)/2$ times. Therefore in the large- N limit, the computational cost of the correlation process is $O(N^2)$. Such a scaling means the monetary cost of large interferometers is dominated by computing hardware. One way to get around this is by choosing a highly redundant array, with antennas evenly spaced on a rectangular grid. Instead of correlating all antennas with one another, the cross-correlation theorem can be employed,

$$\mathcal{F}(\mathbf{x} \star \mathbf{x}^\dagger) = \mathcal{F}(\mathbf{x})\mathcal{F}(\mathbf{x}^\dagger), \quad (1.4)$$

where \mathbf{x} is a vector containing signals from all N antennas. We can then calculate the cross-correlation using only spatial Fourier transforms across the array. Inverse Fourier transforming Eq. 1.4, we can reproduce Eq. 1.1 as follows,

$$\langle \mathbf{x} \star \mathbf{x}^\dagger \rangle = \mathcal{F}^{-1} \{ \mathcal{F}(\mathbf{x})\mathcal{F}(\mathbf{x}^\dagger) \}. \quad (1.5)$$

If the antennas sit on a grid, then the transforms can be computed with Fast Fourier Transforms (FFTs), which scale as $O(N \log(N))$ instead of $O(N^2)$. This was proposed by Peterson et al. (2006) and expanded on in detail by Tegmark & Zaldarriaga (2009). CHIME has such a rectangular array configuration and will be the first large-scale FFT telescope. As we will discuss in Chapters 2 and ??, the FRB experiment will search 1024 formed beams generated by the algorithm described here.

1.2 The time-domain sky

In the early 1930s Karl Jansky built a steerable 20 MHz antenna in order to locate unaccounted-for receiver noise he had been seeing in transatlantic voice transmissions. He found the signal was periodic in sidereal day and established that the radio emission must be of astronomical origin (Jansky, 1933). In doing so he opened up a new window into the Universe. While astronomers had been observing the sky in the optical for millennia, there was now an wholly new slice of the electromagnetic spectrum with which to view the cosmos.

A similar thing could be said about the time-domain sky. Observing temporal rather than spatial fluctuations gives us access to a swath of new sources, and can help us better understand the physics of known sources. Pulsars, which proved the existence

of neutron stars, could not have been discovered without time-series analysis. The first strong observational evidence for blackholes came from X-ray variations of Cygnus X-1 on timescales of days. A subset of these phenomena vary on human-timescales, but seem not to repeat. We call these transients.

Transients are ephemeral events that can last for milliseconds to months. These include gamma-ray bursts (GRBs), supernovae (SNe), and tidal disruption events. They live in the realm of time-domain astrophysics, but are inherently hard to classify due to their fleeting nature. GRBs, for example, were discovered in the 1960s and are still not well understood. In the radio sky, known transients include flare stars, afterglows from supernovae and GRBs, solar bursts, and now FRBs.

1.2.1 Propagation effects

The two time-varying objects we discuss in this thesis are pulsars and FRBs. Since both live well outside of our solar system and both are observed at long wavelengths, one must consider the various propagation effects that occur in the intervening ionized plasma. In the following subsections we introduce the three most prominent effects. These are dispersion, Faraday rotation, and scattering.

Cold plasma dispersion

Electromagnetic waves traveling through a cold dense plasma will undergo dispersion. Here, “cold” refers to the condition that the thermal velocity of the particles in the plasma is much less than that of the wave, i.e.,

$$v_p \gg v_{ion} = \sqrt{2k_B T / m_{ion}}. \quad (1.6)$$

The dispersion results in a frequency-dependent group velocity caused by differential refractive index in an ionized plasma. The refractive index, n , is given by,

$$n = \left(1 - \frac{\omega_p^2}{\omega^2}\right)^{1/2}, \quad (1.7)$$

where ω_p is the plasma's resonant frequency and ω is the electromagnetic wave's frequency. The plasma frequency is

$$\omega_p = \sqrt{\frac{n_e e^2}{4\pi^2 m c}}, \quad (1.8)$$

using e , n_e , and m as the electron charge, number density, and mass respectively. Noting $n = \frac{c}{v_g}$ and plugging this plasma frequency relation into equation 1.7, we can expand about n_e . We get,

$$v_g = c \left(1 - \frac{n_e e^2 \lambda^2}{2\pi m c^2}\right). \quad (1.9)$$

This equation holds for most of the physics described in this thesis, since the dispersive electron plasmas in the IGM, ISM, and even in the remnants of supernovae are relatively diffuse, with plasma frequencies well below the bands in which we observe. For reference, typical values are $n_e^{IGM} \sim 10^{-7} \text{ cm}^{-3}$ (Madau, 2000), $n_e^{ISM} \sim 10^{-2} \text{ cm}^{-3}$ (Lyne & Graham-Smith, 1998) in our Galaxy, and in $n_e^{SNe} \sim 10^{1-3} \text{ cm}^{-3}$ in remnants (see Chapter ??).

For a single pulse, the light travel-time, t , can be written as the integral, $\int_0^D dl/v_g$, into which we can plug Eq. 1.9. The frequency-dependent time delay is then,

$$\Delta t = t - \frac{D}{c} \quad (1.10)$$

$$= 1.345 \times 10^{-3} \nu^{-2} \int_0^D n_e dl \text{ seconds.} \quad (1.11)$$

Here we have switched from angular frequency, ω , to ν in Hz. Dispersion measure (DM) can then be defined as,

$$\text{DM} \equiv \int_0^D n_e dl, \quad (1.12)$$

which is just an electron column density, and is usually reported in units pc cm^{-3} . For a telescope observing between ν_B and ν_T in GHz, the arrival-time difference between the bottom and top of the band will be,

$$\Delta t_{B,T} = 4.15 \times 10^{-3} \text{DM} (\nu_B^{-2} - \nu_T^{-2}) \text{ seconds}. \quad (1.13)$$

While this effect delays all waves with $\nu > \nu_p$, (waves below the plasma frequency will decay exponentially and will not propagate) it is only observationally important for switch sources. Typical pulsars in our Galaxy have DMs between $10\text{-}100 \text{ pc cm}^{-3}$, while DMs can be as high as 2000 pc cm^{-3} for FRBs. The latter gives a dispersion delay of nearly forty seconds between 400 MHz and 800 MHz, where CHIME will observe.

Faraday rotation

If a cold plasma also has a magnetic field, a propagating electromagnetic wave's plane of polarization will be rotated. This is called the “Faraday effect” or “Faraday rotation”, named after the nineteenth century English physicist (Faraday & Martin, 1936). The rotation is caused by circular birefringence, meaning left- and right-circularly polarized light travel at slightly different speeds. Since linear polarization can be thought of as the superposition of a right- and left-handed wave, the result is a rotation of the linear polarization vector.

Like dispersion, this effect is chromatic, depending quadratically on wavelength. The linear polarization vector will be rotated by

$$\phi = 2 \text{RM} \lambda^2 \quad (1.14)$$

where RM is “rotation measure” with units rad m^{-2} . The extent of this rotation depends

on the projection of the magnetic field onto the direction of propagation.

$$\text{RM} = \frac{e^3}{2\pi m^2 c^4} \int_0^L n_e(l) B_{\parallel}(l) dl \quad (1.15)$$

Here B_{\parallel} is the component of the magnetic field vector parallel to $d\mathbf{l}$. RM can be thought of as an electron-density-weighted mean value of the line-of-sight magnetic field between the observer and the source. Conventionally, it is positive for fields directed towards the observer (Manchester & Taylor, 1977).

By dividing Eq. 1.15 by Eq. 1.12 and assuming n_e is roughly constant in whatever medium the radio waves are traversing, one can estimate the average magnetic field in that direction. The ratio of RM to DM is then,

$$\frac{\text{RM}}{\text{DM}} = \frac{e^3}{2\pi m^2 c^4} \frac{\int_0^L n_e(l) B_{\parallel}(l) dl}{\int_0^L n_e(l) dl} = 0.81 \langle B_{\parallel} \rangle \mu\text{G}. \quad (1.16)$$

Therefore one can estimate, with caveats, magnetic field strengths if both RM and DM are measured.

Scattering

The least understood propagation effect in ionized astrophysical plasma is scattering. Scattered radio waves self-interfere constructively and destructively to produce intensity fluctuations (scintillation), temporal broadening, and angular broadening (Manchester & Taylor, 1977). The cause of this multi-path propagation is still greatly contested (Gordreich & Sridhar, 2006; Pen & Levin, 2014). It was assumed to be due to Kolmogorov turbulence, from which one could easily derive the frequency scalings of temporal scattering ($\tau \propto \nu^{-4}$) and angular broadening ($\theta \propto \nu^{-2}$) (Rickett, 1977). Recently, however, this picture has been called into question by pulsar scintillation observations. Stinebring et al. (2001) found parabolic arclets in Fourier-transformed “dynamic spectra” (a 2D time/frequency field) for a number of pulsars, implying that scattering occurs in just

one or two screens and occurs in localized clumps. Irrespective of the underlying physics, scattering is well-studied phenomenologically. It provides a useful tool not just for studying the ISM, but also for understanding the environment of FRBs. We discuss this both in Sect. 1.3 and Chapter ??.

1.3 Fast Radio Bursts

The discovery of fast radio bursts has captivated the attention of astronomers for two reasons: their origin is a genuine mystery, the likes of which had not been seen in transient astrophysics in decades; and the problem appears to be tractable on timescales of years to a decade. There is good reason to think that with the right survey one could at least determine their radial distribution, as well as the nature of the burst source, if not specific details. This is not true of other major contemporary questions. The tensor-to-scalar ratio, r , in inflationary cosmology, or the deviation of dark energy's w from -1, could be constrained with arbitrary improvements without ever making a detection.

The first FRB was discovered in 2007 by Lorimer et al. (2007), and has since been called the “Lorimer Burst”. Its Galactic latitude ($b = -41.8^\circ$) and large dispersion measure ($DM = 375 \text{ pc cm}^{-3}$) implied that the ~ 10 millisecond burst was extragalactic (Lorimer et al., 2007). However, in the years immediately following, no fast transients were seen with DMs exceeding the expected Galactic contribution. This led to skepticism about the celestial nature of the Lorimer Burst and suspicion that it was terrestrial interference (Burke-Spolaor et al., 2011).

Suspicion that this was a one-off event was relinquished with the discovery of four more FRBs in 2010 in the High Time Resolution Universe (HTRU) survey (Thornton et al., 2013). Based on the 23 days of observing with a 0.55 deg^2 beam, they reported a surprisingly large rate of $\sim 10^4 \text{ events sky}^{-1} \text{ day}^{-1}$. Though their detection made a much stronger case for the extraterrestrial nature of FRBs, it was not unequivocally

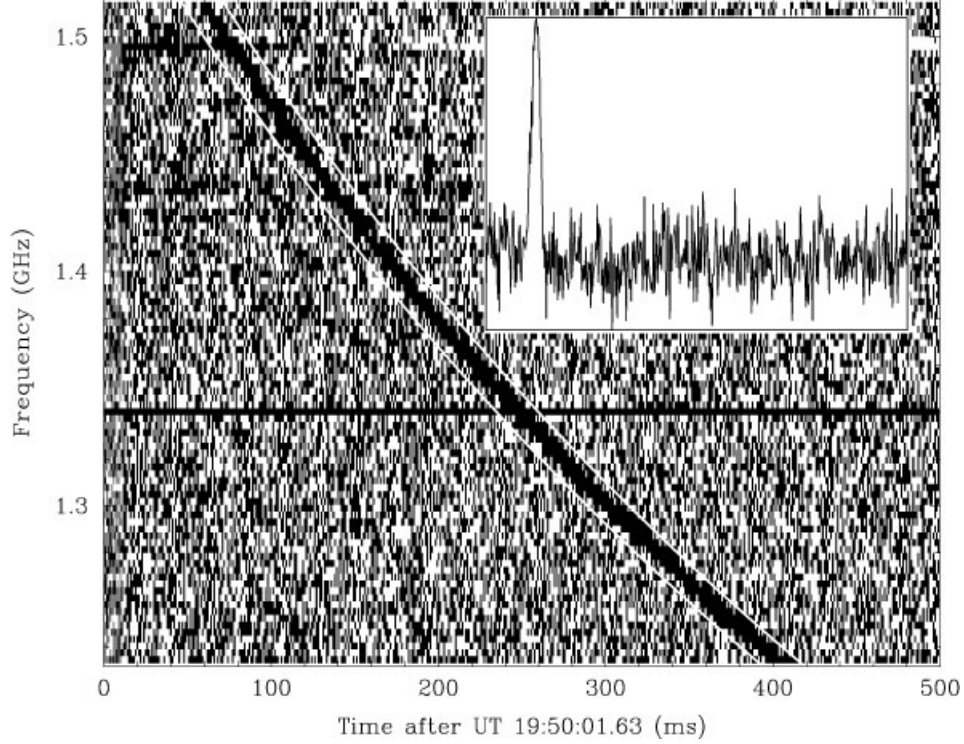


Figure 1.1: Figure reproduced from (Lorimer et al., 2007) of the so-called Lorimer Burst, which is the first known FRB.

accepted. This is because until the discovery of FRB 121102 in Arecibo’s Pulsar ALFA (PALFA) survey, all FRBs had been found with the Parkes radio telescope and in its 13-beam receiver. At Parkes, an unexplained “class” of transients were found in high time resolution data that appeared to be dispersed with hundreds of pc cm^{-3} , and which lasted for ten to a few hundred milliseconds (Burke-Spolaor et al., 2011; Bagchi et al., 2012). These pulses were given the name “Perytons”, named after a mythological hybrid animal.

While an astronomical origin for Perytons was excluded early on due to their multi-beam detections, it was not obvious if they were being emitted in the earth’s atmosphere naturally, or by something human-made (Katz, 2014; Dodin & Fisch, 2014; Danish Khan,

2014). It was later found by Petroff et al. (2015d) that Perytons were likely caused by an on-site microwave oven. The microwave’s magnetron was found to mimic the sweeping λ^2 dependence of truly dispersed sources when the oven’s door was opened prematurely (Petroff et al., 2015d). This made sense given the preponderance of events around local noon, i.e. lunchtime.

In the years since Thornton et al. (2013) discovered their four HTRU bursts, a dozen or so more have been found. These are cataloged online at FRBCAT¹ (Petroff et al., 2016). As we have mentioned, Arecibo’s detection of FRB 121102 ensured that the events were not Parkes-specific. Petroff et al. (2015a) found the first FRB in real-time, as well as the first burst for which there was polarization information. FRB 110523 (Masui et al., 2015) was found in archival data from the Green Bank Telescope (GBT) intensity mapping experiment, which fortuitously saved its data with millisecond time resolution even though it was not strictly necessary for their cosmology. The completed HTRU survey also provided five new sources, found by Champion et al. (2016).

With nearly two dozen detected at the time of this writing, there is still no agreed-upon definition of an FRB. They appear to last for \sim milliseconds, have dispersion measures that are ≥ 2.5 times that of the Galactic contribution (the range has been $375 - 1600 \text{ pc cm}^{-3}$), and maximum flux densities of roughly a Jansky. Exceptions include the Lorimer Burst, which was ~ 30 Jy and is the brightest FRB by far, and FRB 010621 whose DM was only about 1.4 times that expected from the Milky Way (Lorimer et al., 2007; Keane et al., 2012). At both L-band and $\sim 800 \text{ MHz}$, a detectable rate of several thousand each day over the whole sky now seems likely (Connor et al., 2016a; Champion et al., 2016).

Beyond the nebulous definition, our sampling of FRBs is certainly incomplete, as well as our constraints on the properties we measure. Brightness is reported as if the burst were found at the beam’s center, so each published flux is a lower limit. We also do not yet

¹<http://www.astronomy.swin.edu.au/pulsar/frbcats/>

know the DM distribution. There may be a population of events with $DM \approx 10^4 \text{ pc cm}^{-3}$ that are either too rare to see in two dozen bursts, or to which current search algorithms have not been sensitive. Scattering is another poorly constrained parameter. FRBCAT lists five bursts with evidence for scattering, with broadening index around -4, as one would expect (Petroff et al., 2016). However, several sources have been unresolved in time, meaning their width and scattering properties are only constrained from above. The extent and prevalence of scattering is of interest for a couple reasons. One is that it has implications for the source environment, and also because scattering is the limiting factor for low-frequency surveys, like CHIME and LOFAR (Bandura, 2014; van Leeuwen, 2014); an FRB scattered to 10 ms at 1.4 GHz would be several seconds at 400 MHz and effectively undetectable.

1.3.1 Models

Starting with the Lorimer Burst and continuing on to the four high-lat HTRU FRBs, the default assumption was that the progenitors were at cosmological distances (i.e. IGM-induced dispersion). To a lesser extent, the community seemed to assume they did not repeat, in part because of null-result follow up observations that were done (Petroff et al., 2015c), but also because bursts coming from gigaparsec distances might only have enough energy for a single event. It has been argued (Katz, 2016) that the cosmological interpretation is the most economical way of getting such large column densities of free electrons. In reality, up until recently we did not know their radial distance to better than five orders of magnitude. This is because with such a small sample of events, there was no way of knowing whether they were coming from $z \approx 0.5$, from within our Galaxy, or from our atmosphere.

A significant fraction of this thesis will focus on theoretical elements regarding fast radio bursts. Therefore it would be prudent to provide context for both the history of models that have come in and out of the picture, as well as a time-line of the observations

that have informed them. We will start by enumerating the most prevalent theoretical explanations for the origin of FRBs. They will be lumped into two categories: cataclysmic, in which the progenitor is effectively destroyed, and non-cataclysmic. Note that in Chapter ??, table ?? partitions models by their distance and includes each theory's predictions for various observables.

Cataclysmic explanations

- *Blitzars*: Falcke & Rezzolla (2014) suggested that a supramassive neutron star might emit a burst of radio once it has lost its angular momentum and has begun to collapse into a black hole. This collapse will hide the star behind the event horizon and magnetic field lines will snap into place. In this model FRBs do not repeat, since the radio chirp is the object's final signal. The authors also assume these compact objects would be at cosmological distances. Given the known existence of neutron stars with mass greater than the Chandrasekhar limit, Falcke & Rezzolla (2014) conjectured that a few percent of neutron stars are supramassive and rotationally supported, and thereby eventually undergo such a transition. A natural shortcoming of this model is its lack of testable predictions. No electromagnetic counterpart is to be expected, and the proposed gravitational wave counterpart would likely be quite weak.
- *Merging compact objects*: The timescales and energies involved invoke merging compact objects. It has been suggested that NS-NS mergers similar to short-GRBs would satisfy the energetics (Totani, 2013). One might then expect a gamma-ray counterpart. Merging white dwarfs has also been proposed (Kashiyama et al., 2013). It has been suggested that the event rates may not be high enough in these models.
- *Evaporating black holes*: In this model exploding primordial black holes emit energy

at wavelengths corresponding to their Schwarzschild radius, which Barrau et al. (2014) suggest the relation,

$$\lambda_{obs} \propto (1+z) \left(\sinh^{-1} \left[\left(\frac{\Omega_{\Lambda}}{\Omega_M} \right)^{0.5} (1+z)^{-3/2} \right] \right)^{1/4}, \quad (1.17)$$

gives observable wavelengths of \sim centimeters.

Non-cataclysmic explanations

- *Galactic flare stars:* One of the first non-cosmological, non-cataclysmic models for FRBs suggested they were flaring main-sequence stars in our own Galaxy (Loeb et al., 2014). In this scenario, coronal plasma provides the DM rather than the IGM. The authors argue that the heightened energetics required by FRBs at cosmological distances theoretically motivates nearby sources. The model generically predicts repetition and, of course, overlap with known Galactic variable stars (Loeb et al., 2014; Maoz et al., 2015).
- *Magnetar flares:* Within one month of publication of the Lorimer event, Popov & Postnov (2007) had proposed that hyper-flares from cosmological magnetars could give rise to highly energetic millisecond bursts. They suggested that an extragalactic soft gamma-ray repeater (SGR) could be generated in a magnetar magnetosphere due to “tearing mode” instability. The emission mechanism of these “millisecond Extragalactic radio burst (mERBS)”, as they were - and might have ultimately been - called, was described in 2002 by Lyutikov (2002). The model requires a cosmological population to achieve the large DMs and event rates.
- *Supernova remnant pulsars:* In this model FRBs are very young pulsars, in external but non-cosmological galaxies. Their large dispersion measure from free electrons in their supernova remnants, which also Faraday rotates and scatters the burst. The

dispersion measure is given by,

$$\text{DM} \approx \frac{x_e M_{\text{ej}}}{m_p \frac{4\pi}{3} v_{\text{ej}}^2 t^2} \quad (1.18)$$

, where x_e , M_{ej} are the free electron fraction and supernova ejecta mass respectively, v_{ej} , is the ejecta velocity, and t is the age. Proposed by Connor et al. (2016c) as a way of explaining all the observed phenomenology locally, it has been further studied by Piro (2016) and Lyutikov et al. (2016). One firm prediction of this model is that the flux distribution of FRBs will be strictly Euclidean, since their progenitors are in the local Universe ($z \lesssim 0.1$). Further observational consequences of this model, including repetition, are described in ??.

- *Circum-nuclear magnetars:* This model (Pen & Connor, 2015) infers the existence of radio-loud magnetars at the centers of galaxies from the high-DM (1778 pc cm^{-3}), high-RM ($-6.4 \times 10^4 \text{ rad m}^{-2}$) SGR J1745-2900, which is $< 1 \text{ pc}$ from Sgr A*. Galactic centers would therefore provide the dispersive electron plasma and the bursts would not need to be at cosmological distances, similar to the supernova remnant model. The source of the pulse would be a radio-flare from the nuclear magnetar, similar to the mechanism in (Popov & Postnov, 2007). One issue with this model is the dearth of low-DM FRBs; since radio-loud magnetars exist outside of galactic centers, the model demands that the nuclear sources preferentially emit radio flares.
- *Super-giant pulses:* This is a class of models in which FRBs are akin to giant pulses from the Crab, but several orders of magnitude more energetic. The Crab pulsar, which exhibits the highest known brightness temperatures in the Universe, can get up to $\sim \text{MJy}$. Cordes & Wasserman (2016) provided a detailed investigation into the physical limitations of coherent emission around 1 GHz. Connor et al. (2016c) also use super-giant pulses as the source of the radio bursts. In that model, giant

pulses are necessarily brighter earlier in the young pulsar’s life ($\lesssim 500$ years), which explains why we do not see Crab giant pulses as energetic as an extragalactic FRB. Any version of this model would expect repetition.

1.3.2 Empirical constraints

As of early 2014 no FRB observation presented any standout clues about the emission mechanism. They were all observed only in Stokes I and none had been seen to repeat. With FRB 140514, the first real-time detection, full Stokes information was recorded and immediate follow up observations were carried out in other wavelengths (Petroff et al., 2015b). It was found to have $21 \pm 7\%$ circular polarization and negligible linear polarization. No counterpart was found after 12 telescopes from radio to X-ray monitored the FRB field in the days following, ruling out local ($z < 0.3$) SNe and long GRBs (Petroff et al., 2015b).

Between late 2015 and early 2016, there was a rapid succession of significant observational claims. FRB 110523, was the first, published in fall of 2015 (Masui et al., 2015). It was the only burst after FRB 140514 for which polarimetry could be done. It was found with the GBT IM data in archival data, and had $44 \pm 3\%$ linear polarization (Masui et al., 2015). Interestingly, the source was Faraday rotated with an RM of -186 rad m^{-2} , which is roughly two orders of magnitude greater than what would be expected in the IGM (Oppermann et al., 2015). This seemed to put strain on the cosmological interpretation of FRB 110523, since the dispersion (caused by free electrons) and the Faraday rotation (caused by free electrons + a magnetic field), would be coming from two different places.

Another exceptional feature of this event was the evidence for two separate scattering screens. Scintillation was found with a $\sim \text{MHz}$ decorrelation length as well as temporal broadening at millisecond timescales. The μs scintillation is expected arise when the source enters our Galaxy, implying the ms scattering must happen somewhere local to the source (Masui et al., 2015). The FRB also showed a polarization angle swing, similar

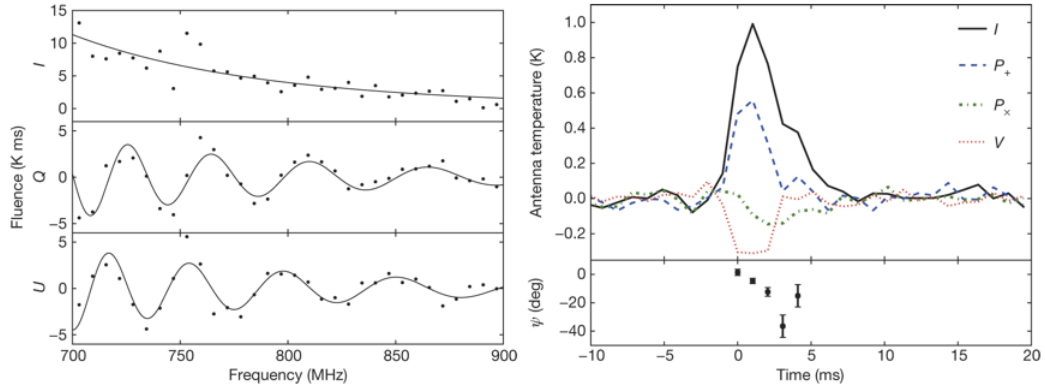


Figure 1.2: Figure adapted from Masui et al. (2015) of FRB 110523. The left panel shows the large Faraday rotation and the right panel shows the dedispersed, frequency-averaged pulse profiles for total intensity, Stokes V, and the two linear polarizations. One can also see the polarization angle swing across the burst.

to that seen in pulsars, indicative of a rotating object. These facts, along with constraints on the dispersing electron’s plasma frequencies, ruled out Galactic models. They also lent credence to rotating neutron star models, whether magnetar flares or supergiant pulses from young pulsars.

Another major claim was made by Keane et al. (2016), who found a host galaxy at $z = 0.492$ that appeared to be associated with an FRB. The localization was not based on a VLBI observation, but rather a coincident radio “afterglow” in the same $\sim 13''$ Parkes field. Part of a multi-wavelength follow up, the Australia Telescope Compact Array (ATCA), observing at 5.5 and 7.5 GHz, found a radio source whose flux seemed to fall off a factor of a few in roughly 6 days. The authors interpreted this as a fading transient, not unlike radio afterglows of short GRBs, favouring the compact object merger

scenario. However, the validity of this galaxy’s association with the FRB has been called into question. Shortly after the press release of (Keane et al., 2016), Williams & Berger (2016) did a further observation suggesting the source was in fact a *variable* rather than a transient, the latter of which are quite rare.

By far the most important new observation in the field is the discovery of FRB 121102’s repetition (Spitler et al., 2016). 121102 was found to repeat 10 times in (Spitler et al., 2016) and 6 additional times in (Scholz et al., 2016). With one fell swoop the numerous models in the cataclysmic class were falsified. The exception being if there are two or more populations of FRBs with disparate progenitors, in which case “Type A FRBs”, for instance, are known to be non-destructive. The sub-bursts were all also detected with Arecibo, many of them getting down to the telescope’s fluence limit, implying most of its bursts were undetectable (Spitler et al., 2016; Scholz et al., 2016). Its DM changed by less than measurement uncertainty of $\sim 6 \text{ pc cm}^{-3}$ over the course of several years, though the spectral properties varied wildly from burst to burst. Finally, its repetition was highly non-Poissonian, with 6 of the first 10 appearing in single twenty minute pointing, despite monitoring the field for over ten hours. Such non-Poissonian behaviour was predicted in (Connor et al., 2016b) and has consequences for survey strategy.

1.4 Thesis Outline

This thesis is organized into five main chapters, some of which have been adapted from published papers. In Chapter 2 we introduce the Canadian Hydrogen Intensity Mapping Experiment (CHIME). We start by describing the science goals of the telescope’s three back-ends: cosmology, pulsar, and FRB. The instrument is discussed, including a step-by-step outline of the signal chain. This chapter’s purpose is to provide context for the other chapters, which either involve CHIME directly or are relevant to its science. Also presented is early analysis work that I have done, including the discovery of various unex-

pected beam properties of the CHIME Pathfinder. A simple simulation of aliasing with a 128-feed cylinder is described, which I built. However, since this is a large collaboration, most of the work in this chapter was done by other members of CHIME. For example, the F-engine was built by Kevin Bandura, Jean Francois Trempe, and Matt Dobbs, but it still seemed necessary to describe that step in the data processing. Richard Shaw, Ue-Li Pen, and Kris Sigurdson developed the “m-mode” formalism and pipeline, but it is essential to the science of CHIME cosmology. Details about the instrument in this chapter overlap with the work published in (Bandura, 2014), (Newburgh et al., 2014), and (Berger et al., 2016), all of which I co-authored.

In Chapter ?? we delineate the commissioning of CHIME Pathfinder’s beamformer, prefaced by a mathematical introduction to digital beamforming. The work described was done largely by myself, but with the aid of several key people. Andre Recnik was instrumental in networking and miscellaneous computing issues related to the back-end. My co-supervisor, Keith Vanderlinde was critical in guiding this project in the right direction. The real-time FRB VLBI survey, starting with the burst-search that was attached to the Pathfinder’s formed-beam, relied on the direction of my other co-supervisor Ue-Li Pen and the programming of Kendrick Smith and Kiyo Masui. Kendrick wrote a mutli-threaded real-time VDIF packet assembler, and Kiyo wrote a tree-dedispersion burst search in `Python`.

Chapter ?? presents a theory for the origin of FRBs in which the bursts are from extragalactic but non-cosmological pulsars in the remnants of recent supernovae. We published this model in Monthly Notices of the Royal Astronomical Society (MNRAS) at a time when FRBs were not known to repeat and most authors assumed they were cosmological and cataclysmic (Connor et al., 2016c). This work was done in collaboration with Ue-Li Pen and Jonathan Sievers. It was Jonathan Sievers’ idea to place FRBs in young, compact SNe remnants. I then built a model to represent that environment, infer its consequence, and feasibility in terms of event rate and energetics. With Ue-Li I also

worked on the observables of the supernova remnant hypothesis as well as other models. These are included in table ??.

Chapter ?? is called “FRB Statistics”. In it we analyze a number of statistical problems that have come up since the discovery of FRBs. These include their purportedly non-uniform latitudinal distribution and constraints on their repeat rate. These sections were adapted from a paper published in MNRAS in collaboration with Ue-Li Pen and Niels Oppermann (Connor et al., 2016b). My contribution to this paper included building a model for FRB repetition based on $1/f$ noise and doing mock-follow-up Monte Carlo simulations. Working with Ue-Li, I also developed a test for the latitudinal dependence of the burst-rate that is based on a biased coin flip. This chapter later investigates the all-sky event rate below L-band, and forecasts for CHIME FRB and several other low-frequency experiments. The corresponding sections were derived from (Connor et al., 2016a), again published in MNRAS. As lead author I carried out most of the calculations, excluding the frequentist/Bayesian estimates for event rate, which were conceived of by Niels Oppermann. Hsiu-Hsien Lin and Kiyo Masui, who are members of the GBT IM experiment, provided details about the survey and its dataset. Ue-Li Pen was crucial in the overall direction of the research, particularly in focusing on easily calculable statistics and the idea to forecast by comparing similar surveys. The final paper whose work ended up in Chapter ?? was (Oppermann et al., 2016), accepted to MNRAS. This work was regarding the signal-to-noise distribution of FRBs and the use of a V/V_{\max} -test. Niels Oppermann created the plots and wrote code to calculate the α /event-rate posterior, but most of the theoretical work was done in meetings with Ue-Li Pen, myself, and Niels.

The final chapter investigates the sub-millisecond structure of individual pulses from B0329+54. The “microstructure” is studied in full polarization, and its quasi-periodicities are found to be common within a pulse for all Stokes parameters, but not common between pulses. This work was done with the supervision of Ue-Li Pen, who provided physical insight and guidance on the project’s direction.

Chapter 2

The Canadian Hydrogen Intensity Mapping Experiment

2.1 Chapter Overview

In this chapter we will introduce in detail the Canadian Hydrogen Intensity Mapping Experiment (CHIME). The chapter's purpose is to give context for the subsequent thesis chapters, for which CHIME is highly relevant. We will discuss the science that motivated its construction, namely an attempt at mapping out the Universe's hydrogen in order to do large-scale structure (LSS) and learn about dark energy. The science goals of the two time-variable back-ends will then be introduced, with an emphasis on CHIME-FRB, whose objectives are most relevant to this thesis. Finally, we will describe the instrumentation that unifies the three projects. We will discuss the early data analysis and instrumental characterization of the Pathfinder, including the pervasiveness of a standing-wave between our reflector and the focal line, and the mis-pointing of our beams due to a $\sim 2^\circ$ azimuthal rotation of our cylinders.

2.2 Introduction

CHIME is a Canadian collaboration between the University of British Columbia (UBC), the University of Toronto (UofT), McGill University, and the Dominion Radio Astrophysical Observatory (DRAO). Located at DRAO — Canada’s national radio observatory seen in Fig. 2.3 on page 25 — CHIME consists of two stages of development. The first is a pathfinder instrument, known henceforth as the CHIME Pathfinder, which is two 20x37 m cylinders and is shown in Fig. 2.1. The second is the final instrument, called either full CHIME or just CHIME, and consists of four 20x100 m cylinders. The Pathfinder was first “on sky” in November 2013, however it has only been observing in full capacity, i.e., with all of its feeds mounted and drawing power, since 2015. As of late spring 2016, full CHIME’s structure exists and is meant to be instrumented before the end of 2016. It can be seen in Fig. 2.2.

CHIME’s primary science goal is to measure the Universe’s neutral hydrogen between redshifts 0.8-2.5, mapping out the large-scale structure (LSS) and constraining dark energy’s equation of state. However, it was noticed early on that CHIME could be a powerful tool for studying the time-variable sky. Fortunately, digital radio telescopes like CHIME can run multiple experiments in parallel, since data can be siphoned off and cloned between different back-ends. In light of this an effort was made, successfully, to acquire funding for two new experiments to piggy-back on CHIME. One is a pulsar back-end that will monitor large numbers of sources each day, observing up to 10 pulsars at a time, 24/7. Another is an FRB back-end that will search 1024 FFT-formed beams for dispersed transients.



Figure 2.1: Photograph of the CHIME Pathfinder, constructed in 2013. The Pathfinder was built as a testbed for analysis and instrument design, largely because CHIME is attempting a very difficult measurement that requires an unprecedented understanding of our telescope. In attempting a new technique (21 cm intensity mapping) with an unorthodox telescope design we were guaranteed to not get it perfect the first time, hence the smaller precursor instrument to “find the path”. After two years of taking data in multiple configurations, we have learned a number of lessons about calibration, cross talk, our beams, and the correlator. We also ran into unforeseen obstacles, including a mis-pointing caused by ambiguity in the definition of “north”, the pervasive effects of a standing wave between the reflector’s vertex and our focal line, and the impact of surface perturbations in the cylinders’ mesh.

2.3 CHIME Science

2.3.1 21 cm Cosmology

Historically, constraining the nature of dark energy has been expensive in time and resources. The most promising method has been to map out the Universe’s matter at large scales and at many different redshifts, to measure its expansion with the baryon acous-



Figure 2.2: Full CHIME shortly after the construction of the fourth and final parabolic cylinder in fall 2015. Each dish is 20 m in the east-west direction and 100 m long. Unlike the Pathfinder, the cylinders are aligned with the *celestial* North Pole and should have true declination beams. There was also great care taken creating a smooth surface, since the Pathfinder’s relatively large surface RMS led to issues with its beams.

tic oscillations (BAOs) (??). Traditional spectroscopic galaxy surveys require resolving scales (of galaxies, specifically, ~ 10 s of kpc) that are much smaller than the LSS, in particular the BAO, which is ~ 100 Mpc. A far more economic, albeit precarious, approach is to map out 21 cm emission from hydrogen that traces the underlying dark matter distribution (?Peterson et al., 2006). This technique was proposed as a cheaper and more efficient alternative to galaxy surveys for probing dark energy, and it was given the name “intensity mapping” (?). Since we are concerned only with \sim degree angular scales, the collective emission from thousands of galaxies can be used as a proxy for the Universe’s LSS. 21 cm cosmology therefore opens up access to a huge number of density modes and is in line to take the baton from the CMB as our greatest source of cosmological information (??Tegmark & Zaldarriaga, 2009).

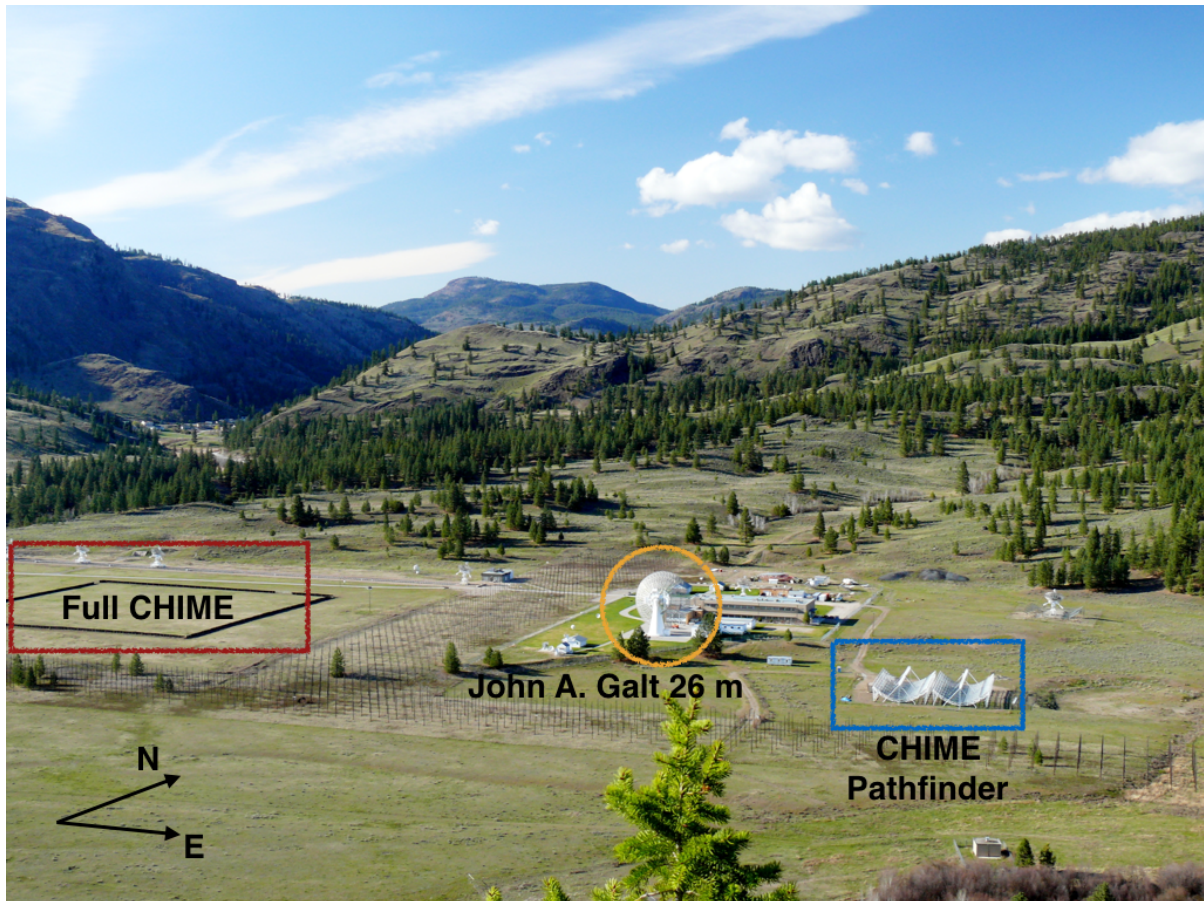


Figure 2.3: The Dominion Radio Astrophysical Observatory (DRAO) in Penticton, British Columbia. The site hosts three dishes relevant to CHIME. One is the CHIME Pathfinder, seen in the bottom right (east-most corner) of this image. Another is the John A. Galt 26 m telescope, which is a steerable equatorial telescope that is used for holographic beam mapping of both full CHIME and its pathfinder. Finally, the site of the full four-cylinder instrument, which was not constructed at the time of this photograph but is now in the west-most field.

In principle, intensity mapping gives us access to large volumes of the Universe, and therefore cosmic variance limited constraints on dark energy’s equation of state parameter w . However, like many high-reward, low economic-cost techniques, measuring LSS with 21 cm mapping comes with a number of systematics. Terrestrial radio frequency interference (RFI) is ubiquitous, meaning long-wavelength measurements will always be

contaminated by human communication in the radio. But fundamentally, intensity mapping is difficult because the redshifted HI emission that contains the cosmological information is faint. After cosmic reionization, neutral hydrogen is confined to galaxies and has a brightness temperature of just a few hundred μK (?). Radio foregrounds below 1.4 GHz can be 10^3 - 10^5 times brighter than this cosmological 21 cm signal (??). They include Galactic synchrotron, extragalactic point-sources, and to some extent, bremsstrahlung.

The signal of interest must therefore be extracted from underneath the loud foregrounds. This would be impossible if it were not for the spectral nature of these foregrounds: Since synchrotron radiation is the sum of a continuous distribution of large numbers of relativistic electrons with different energies, the resulting spectra are smooth and well-characterized by a power-law (?). On the other hand, 21 cm emission is not spectrally smooth since each frequency corresponds to a different redshift and therefore a different patch of neutral hydrogen along the line of sight. One can take advantage of this difference by separating the smooth and rough frequency components of the signal, and there have been numerous attempts at doing this effectively (?????).

?? developed a statistically optimal method known as the “m-mode formalism” for foreground removal and map-making in the presence of beam uncertainties and polarization leakage. Though it was developed with CHIME in mind, it can be applied to any transit interferometer. It was found by ? that one caveat of this method is that one’s telescope must be characterized with an unprecedented level of precision. Complex gains must be tracked with regular cadence, and we must know our full-polarization beams very well. In Sect. 2.4.4 we detail our attempts at this characterization on the Pathfinder.

Once CHIME is calibrated at the level where foregrounds can be removed, it will go after the redshifted 21 cm emission between $z = 0.8 - 2.5$, corresponding to a band of 400-800 MHz. CHIME is constructed to measure angular scales on the sky that best constrain the matter power spectrum at modes corresponding to the BAO. The BAO’s first peak (i.e. the largest spatial mode) appears at $1.35-3^\circ$ for redshifts 0.8-2.5. The smallest scales

that need to be detected are set by the third peak. In the transverse direction on the sky, this sets our array’s physical size of ~ 100 m. In the radial direction, this sets our frequency resolution. The Pathfinder is projected to be able to do interesting cosmology, though it will have to do so with only the first BAO peak due in the transverse direction because of its limited spatial resolution. These parameters are shown in Table 2.4.

2.3.2 CHIME-pulsar

CHIME’s collecting area and wide bandwidth make it a highly sensitive telescope for pulsar astronomy. On top of this, its ability to record data 24 hours a day, 365 days a year, allow for pulsar monitoring that cannot be done elsewhere. Although the existing analog chain can be used for pulsar astrophysics, the required time-domain signal processing is such that a new digital back-end must be built. This will include, for example, a maser for precision timing, a separate GPU cluster for brute-force beamforming, and real-time pulsar processing like coherent dedispersion and folding.

Full CHIME will have the sensitivity to see almost every known pulsar in the northern hemisphere, every single day. This is shown in Fig. 2.4. Access to any pulsar for 10-15 minutes each day will make CHIME a world-class instrument for pulsar astrophysics. Perhaps the most promising avenue for this back-end is the potential to do long-term timing of millisecond pulsars. Pulsar timing can detect or provide interesting new limits on gravitational waves in a frequency-range inaccessible to experiments like LIGO. It will be included in the NANOGrav consortium and will be able to monitor the daily changes in dispersion measure, which is a significant source of error in pulsar timing arrays.

Beyond timing, CHIME will be able to go after any pulsar variation science that takes places on timescales greater than a day, and shorter than ~ 10 minutes. It could carry out scintillation studies, Faraday rotation measure monitoring, and even pulsar searching.

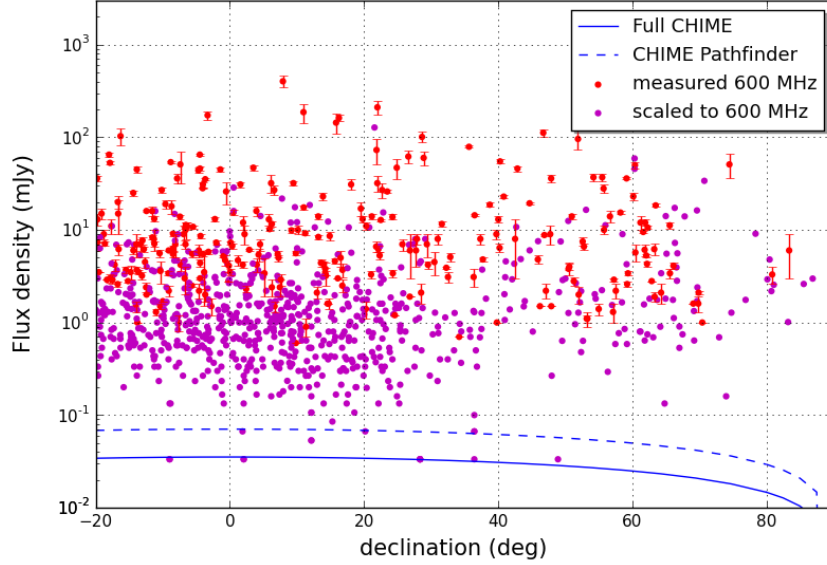


Figure 2.4: Daily sensitivity of CHIME and the Pathfinder for all known pulsars above declination of -20° . The red points have been measured directly in the middle of our band, and the magenta dots are extrapolated from other frequencies.

2.3.3 CHIME-FRB

The origin of fast radio bursts is presently one of the greatest mysteries in the radio sky. Although we have known about them for nearly a decade, fewer than two dozen have been discovered. CHIME, with its $\sim 150 \text{ deg}^2$ FoV could potentially detect this many in its first week on sky. That is because CHIME’s evenly spaced feeds enable us to spatially FFT the array in order to form fan-beams that populate its entire primary beam. This basic idea can be found in (Peterson et al., 2006) and was given the title “Fast Fourier Transform Telescope” in (Tegmark & Zaldarriaga, 2009). By taking advantage of a regularly gridded array, the $N \log N$ scaling of FFTs can be exploited. All N independent beams can then be searched for dispersed radio transients as long as the search is done quickly. For this, a tree-dedispersion algorithm was developed (after being rediscovered — see (?)) that has a computational complexity $O(N_t N_\nu \log N_{DM})$ instead of $O(N_t N_\nu N_{DM})$ like the standard direct method. An example of this is shown in Fig. 2.5 in which the top map shows the response on the sky of a single dipole on the focal line, and the bottom map shows the

result of FFT-beamforming. The beam was simulated by taking the simple dipole beam from (?) and propagating it onto the sky by solving the Fraunhofer diffraction problem.

Just like the cosmology and pulsar back-ends, the FRB survey will be on sky at all times. It will form 1024 Stokes I beams, excise RFI, and search a multi-parameter space in real-time for bursts. The search space includes DM, arrival time, spectral index, width, and a scattering measure. Triggers will then be stored at \sim millisecond cadence with the option of storing baseband, allowing for polarization studies and high time resolution information.

Given its large FoV and substantial collecting area, CHIME is expected to see more FRBs than any other survey. In chapter ?? we forecast the speed of CHIME-FRB and find its rate to be,

$$N_{\text{CH}} \approx 7.5 \left(\frac{50 \text{ K}}{T_{\text{sys}}} \right)^{1.5} \text{ day}^{-1}, \quad (2.1)$$

with a 95% confidence interval of 2-40 per day. This means 10^{3-4} after just one year. With such a large collection of events one could do population statistics on their $N(S)$ distribution, DM statistics, scattering properties, etc. Having \sim 20-arcminute localization for hundreds or thousands of bursts could also be used to correlate with the large-scale structure. Polarization could also be an important feature, which CHIME will have the option to study. For example, one might find significant Faraday rotation is a generic property of FRBs. Large rotation measure (RM) is not explicable by the IGM alone, so the distribution of RMs could tell us about the magnetized environment near the source.

2.4 Instrument

CHIME is a novel telescope that carefully pairs its signal processing and analysis pipeline with its instrumental specifications. It is a cylindrical radio interferometer aligned in the north-south direction with no moving parts. As a transit telescope, it looks at the

	Pathfinder	Full CHIME
Geometric area	1,480 m ²	8,000 m ²
Frequency	400-800 MHz	400-800 MHz
Redshift	2.5-0.8	2.5-0.8
Beamsize	2.5°-1.3°	0.43°-0.22°
No. cylinders	2 (20x37 m)	4 (20x100 m)
No. dual-pol antennas	128	1024
No. tracking beams	1	10
No. FFT beams	undecided	1024
No. freq channels	1,024	1,024 (cosm, psr), 16,384 (frb)
E-W FoV	2.5°-1.3°	2.5°-1.3°
N-S FoV	~100°	~100°
Receiver Temperature	50 K	50 K

Table 2.1: CHIME Parameters

meridian as the earth rotates and the sky passes overhead, and has an on-sky duty-cycle of 100%. Since its reflectors are parabolic cylinders, light is focused only in the east-west direction, with a transverse beam-width given by $\frac{\lambda}{D_{EW}}$, or a couple degrees. In the north-south direction the dish effectively acts as a flat mirror. This results in a large beam that can see nearly the whole north-south sky, barring the antenna’s beam and cosine projection at low-elevation. To gain north-south spatial resolution, CHIME’s focal line is populated with broad-band, dual-polarization antennas that we call “clover” feeds due to their four pedals, shown in Fig. 2.6. The signals from these feeds can be interfered either in beamforming or by traditional interferometric correlation in order to obtain north-south spatial resolution.

2.4.1 Clover-feeds

The feed petals are made from printed circuit boards (PCB) (?). The balun and support going up to the backplane are made from Teflon-based PCB in order to minimize loss. Electrical loss is also reduced by removing all material from along the slot transmission. The clover feeds are distributed along the focal lines in groups of four, mounted to steel

“cassettes”, each of which contains one power source and electronics for thermometry. This focal line configuration can be seen in Fig. 2.6.

Aliasing

The feeds are separated by ~ 30 cm, constrained by their physical size and the requirements of a 400-800 MHz feed. This is problematic for the top of our band. Since we observe at 37.5-75 cm, wavelengths shorter than twice the physical separation of our feeds will not be properly Nyquist sampled. Therefore below ~ 60 cm (above ~ 500 MHz) we do not uniquely measure the electric field in the north-south direction and our signal will be aliased. In other words, without further information, a point source’s declination will be ambiguous at high frequencies at any given time. An example of this is shown with a simulated formed beam shown in Fig. 2.7.

2.4.2 Amplifiers

After light bounces off the reflector and couples to the clover feeds, the signal is amplified by low-noise amplifiers (LNAs) attached directly to the antennas at the focus. The LNA’s noise figure across most of the band is ~ 35 K (Bandura, 2014). The LNA is noise matched rather than impedance matched, resulting in a relatively large reflection coefficient.

The signal is then sent through ~ 60 m of coaxial cable down the cylinder’s central strut and into the correlator Sea Can, within which there is an RF-shielded room containing all of the correlator hardware. The Pathfinder’s 256 channels are then passed through a second stage of amplification in the filter amps.

2.4.3 Correlator

Both the Pathfinder and full CHIME have “FX” correlators, meaning the signal is first Fourier transformed and then correlated. On the Pathfinder, the signals from the 256 feeds are split up and sent to the F-engine where a polyphase filterbank (PFB) is applied.

The PFB channelizes the signal. It is similar to a Fourier transform, except that it mitigates channel-to-channel leakage in the presence of strong RFI. All channels must then be brought back together for the full N^2 correlation, so each of the 16 GPU nodes gets one sixteenth of all frequencies. A similar digital back-end will exist for CHIME, but scaled up, with 256 GPU nodes.

F-engine

The CHIME Pathfinder’s F-engine consists of 16 custom FPGA boards, each with 16 ADCs, which sample the analog signal at 800 MSps at 8 bits and channelize the data into 1024 frequency bins (?).

X-engine

The correlation component of CHIME’s back-end is a custom GPU-based cluster of consumer-grade AMD cards (?). The Pathfinder X-engine is made of 16 nodes, each containing three AMD R9-series GPUs. 6 of the nodes are water-cooled and 10 of the nodes are air-cooled. The cluster is one of the largest such systems in operation, correlating 32,896 input pairs and 1024 frequency channels over the 400 MHz of bandwidth. Its kernels are written in OpenCL.

2.4.4 Beams

CHIME’s design and analysis approach has forced the collaboration to wager that it will be able to understand its instrument exceedingly well. ? showed that in order to recover a largely unbiased powerspectrum after foreground removal, beam-widths must be known to 0.1%, and complex gains must be known to 1% each minute. Their analysis was based on simulation and a simple proxy for beam characterization (namely width in one dimension), but ultimately we will have to understand the whole 2D beam at each frequency and for all antennas.

Our approach to calibration is described in (Newburgh et al., 2014). For beam-mapping, a technique known as holography is being used whereby a steerable secondary telescope tracks sources as they drift through the CHIME beams. By correlating the tracking telescope (in our case the 26 m John A. Galt antenna) with the CHIME feed, one can pull out the CHIME feed’s electric field response. This gives both the amplitude and phase of all beams on the array for an hour angle track of constant declination, and also eschews the confusion issue that comes from having such a large beam. For reference, see the top panel of Fig. 2.5.

Cylinder rotation

Before a full-fledged holography programme could commence, we began to learn about our beams through the transits of bright point-sources. Shortly after the Pathfinder saw first light, we noticed point-sources were transiting at different times than we might expect. This phenomenon seemed to be declination-dependent, with objects north of zenith arriving late and objects south of zenith arriving early. We found this to be due to a 1.96° cylinder rotation in the positive azimuthal direction. This was caused by miscommunication about the conversion between Universal Transverse Mercator (UTM) and Geographic coordinates, i.e. the use of easting/northing with latitude/longitude.

Frequency dependence

A more difficult phenomenon to explain, which we also discovered in early point-source transits, was an ever-present ~ 30 MHz ripple in our frequency beams. 30 MHz is the frequency of a wave with length ~ 10 m, which is what one would expect from a 5 m standing wave between the vertex of our cylinder’s reflector and the focal line. This standing wave was found to cause a ripple in our beam’s full-width half maximum (FWHM) of order 30%, as can be seen in Fig. 2.9.

Frequency ripples in our beam-widths or forward gain caused by intra-reflector bounces

might have been predicted, as it has been seen in other telescopes (e.g.). However, shortly after the Pathfinder began taking data steadily, we noticed a more confounding issue: Oscillation in frequency of the pointing of our beams. On top of the declination-dependent mis-pointing of our beams, we also discovered a pointing oscillation in frequency with a period of 30 MHz. Strong, sinusoidal frequency-dependent pointing seems to be a novel issue. This is shown in Fig. 2.10. At first this pointing wander was hard to explain, since it seemed to require a systematic east-west asymmetry. The only obvious directionality in the system was the fact that in a two-dish system, there is a cylinder walkway on one side and not the other. However, simulations showed that a bounce between focal lines produces an effect that is several orders of magnitude too small.

It now seems that the combination of a relatively large surface root-mean square (RMS) on the Pathfinder’s reflector, along with two or more bounces between the dish and the focal line, can lead to centroid wander. The system was simulated using antenna modeling software **GRASP**, using a randomly deformed reflector and a second bounce.

2.5 Conclusion

The Canadian Hydrogen Intensity Mapping Experiment is an innovative telescope that will do ground-breaking research at a cost that is a small fraction of the budgets of comparable experiments. We have taken advantage of Moore’s law by building a static reflector and attaching to it powerful computing back-ends. The GPU-based correlator, along with CHIME’s regularly-spaced antennas and rectangular grid, allows it to be the first large-scale operational “Fast Fourier Transform Telescope”.

In this chapter we have introduced its primary science goal, 21 cm intensity mapping, and discussed the systematic issues that make measuring the BAO in hydrogen so arduous. It was also shown why CHIME makes for a powerful probe of the time-variable

radio sky. Fast radio bursts have remained a mystery for nearly a decade, and yet fewer than two dozen have been observed. CHIME’s hundred-square-degree FoV and its ability to populate that large primary beam with searchable formed beams will unequivocally make it the fastest survey in the near future. This will allow for unprecedented population statistics, polarization studies, and cross-correlation with galaxy surveys to aid in localization. The pulsar back-end will provide the NANOGrav pulsar timing array with daily DM monitoring of millisecond pulsars. It will also allow for pulsar studies of any timescale shorter than ~ 15 minutes and longer than one day.

Though the three experiments are going after distinct science and have different digital back-ends, they share everything upstream of the correlator. In Sect. 2.4 we outlined the analog chain for the Pathfinder, as well as the digitization and channelization that takes place in the F-engine. Aliasing is inevitable for the part of our band where wavelength is shorter than twice the feed spacing. This effect is simulated in Fig. 2.7.

We also present some of the early findings of Pathfinder calibration, particularly with respect to the beams. Most of the Pathfinder data analysis will be presented in chapter ??, but here we have summarized some of the more puzzling aspects of our instrument, deduced largely from the transits of bright point sources. The cylinders seem to be rotated by 1.96° in the azimuthal direction, with respect to true north. This results in beams that do not quite trace the meridian, and therefore objects transit at hour angles different from their right ascension, in a declination-dependent way. We also found frequency dependence in our beams. A 30 MHz interaction between the focal line and our cylinder’s vertex (a 5 m distance) results in a \sim degree-ripple in our FWHM as a function of frequency. This standing wave, along with relatively large perturbations in the mesh-surface of our reflector, give rise to beam wander as a function of frequency. These two effects are shown in Fig. 2.9 and Fig. 2.10, respectively.

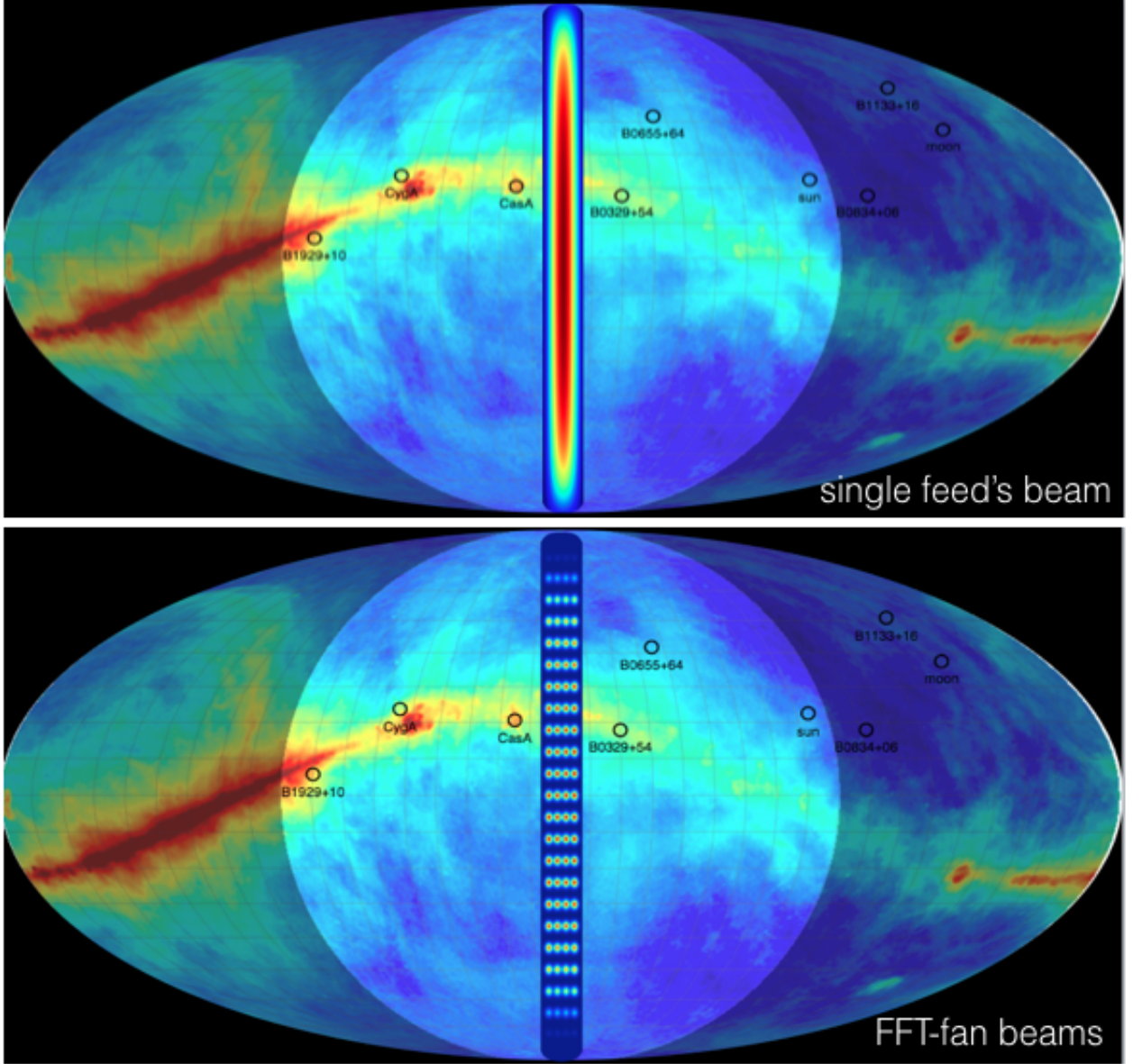


Figure 2.5: *top panel:* The simulated on-sky response of a single feed on a CHIME cylinder, plotted over the ? map at 408 MHz in ground coordinates. The brightened circular area shows the above-horizon region at DRAO at a local sidereal time of roughly 1h30m00s. *bottom panel:* The on-sky response after FFT-beamforming of the array with feeds populated along all four CHIME cylinders. In this setup each cylinder only has 24 feeds, though the real instrument will have 256. This helps visualize the number of independent modes CHIME can measure at a given time, since the final synthesized fan-beams contain the same information as the full N^2 correlation. These FFT-beams are also what will be searched in the FRB back-end. A multi-parameter search will be run in real-time on the 1024 Stokes I beams formed in the FRB back-end, with the ability to write to disk baseband information for polarization studies.



Figure 2.6: Photograph of eight clover feeds on the CHIME Pathfinder. They are separated by ~ 30 cm and mounted in groups of four on cassettes containing each feed's electronics, as well as house-keeping instrumentation. The focal line is 5 m above the reflector.

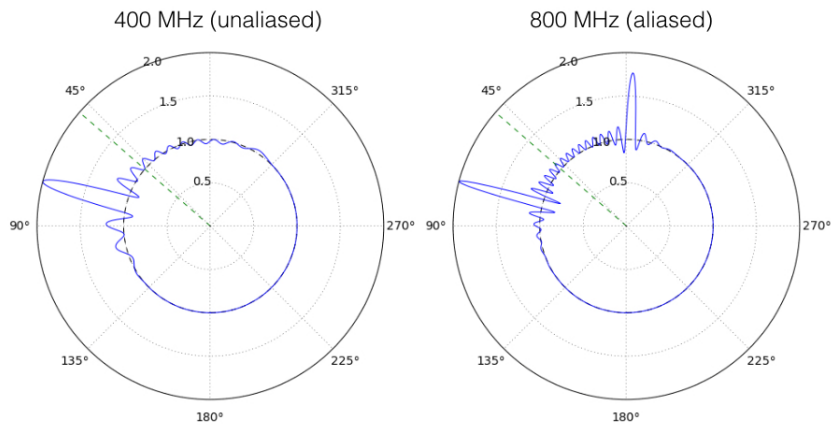


Figure 2.7: A demonstration of aliasing at short wavelengths, based on a simple simulation. In both polar plots (400 MHz left, 800 MHz on the right) a beam is formed at a $\sim 70^\circ$, effectively giving the array's response in that direction. At high frequencies the signal is aliased: One cannot differentiate between the location on which the beam was formed and the pixel at $\sim 350^\circ$.

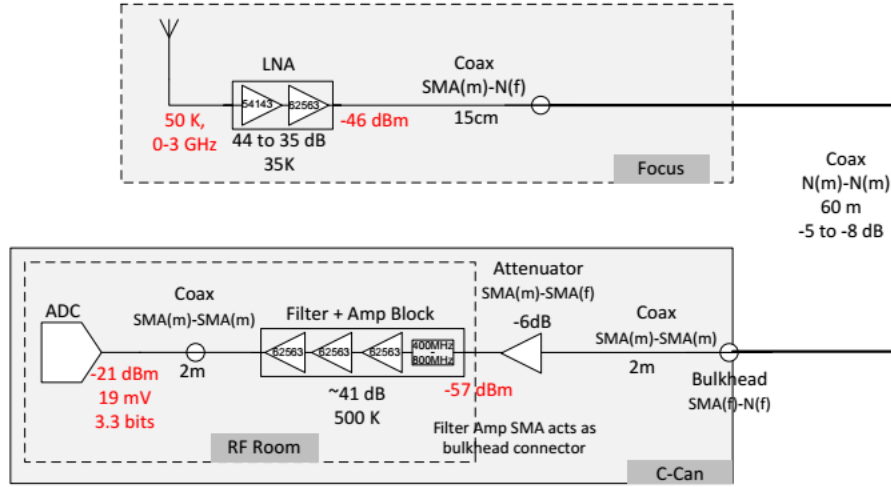


Figure 2.8: Diagram of the CHIME Pathfinder analog chain taken from (Bandura, 2014). The sky signal is amplified in the LNA block by 35–44 dB across the band, adding ~ 35 K of noise. It is then sent across roughly 60 m of LMR-400 coaxial cable to an RF-shielded room. The signal is attenuated, then bandpass filtered over the 400–800 MHz band. It is amplified again by ~ 40 dB in the FLAs before being digitized in the ADCs.

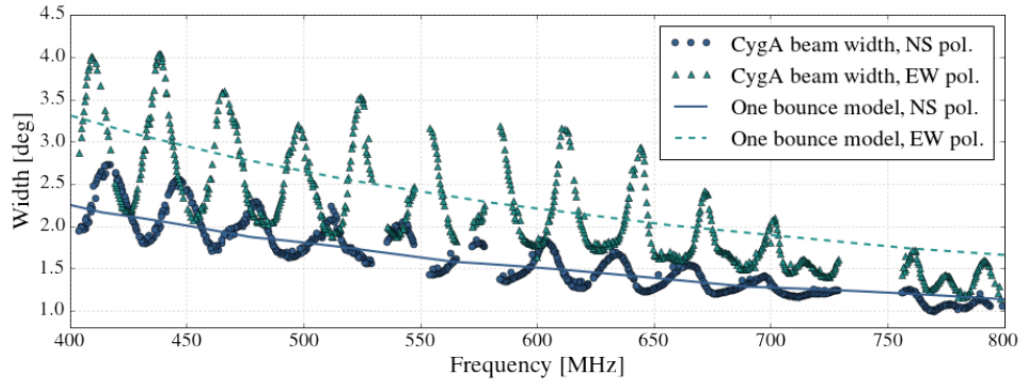


Figure 2.9: Beam full-width half maximum vs. frequency for a single dual-polarization CHIME Pathfinder antenna, based on the Gaussian fits to a Cygnus A transit. The turquoise triangles are the data for the east-west polarization and the blue circles are the north-south beam. Over-plotted in dashed and solid lines are the model. The true beam-widths show a drastic 30 MHz oscillation, resulting in nearly a 2° difference between ~ 420 MHz and ~ 445 MHz. This implies an interaction between the focal line and the reflector, whose vertex is 5 m below the feeds. The model is based on the feed’s beam, which accounts for the different in antenna beams of the two polarizations. It assumes no standing wave and no surface perturbations, which is why the expected ν^{-1} is produced without any frequency ripple.

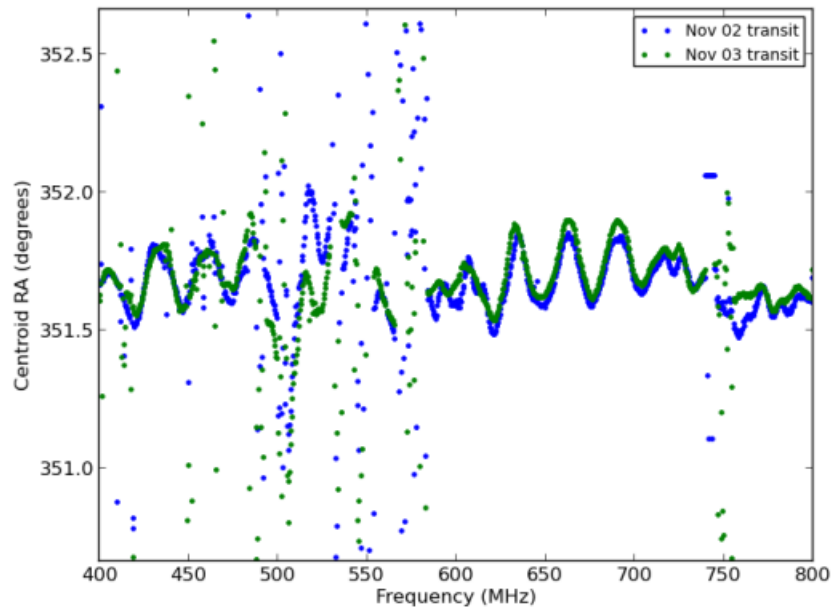


Figure 2.10: A periodic variation of the primary beam centroid for a single Pathfinder feed, measured with a transit of Cas A. Especially between 600-725 MHz, one can see a sinusoidal 30 MHz oscillation in pointing by as much as 20 arcminutes.

Bibliography

Bagchi, M., Nieves, A. C., & McLaughlin, M. 2012, MNRAS, 425, 2501

Bandura, K. e. a. 2014, in Society of Photo-Optical Instrumentation Engineers (SPIE) Conference Series, Vol. 9145, Society of Photo-Optical Instrumentation Engineers (SPIE) Conference Series, 22

Barrau, A., Rovelli, C., & Vidotto, F. 2014, Phys. Rev. D, 90, 127503

Battye, R. A., Davies, R. D., & Weller, J. 2004, MNRAS, 355, 1339

Berger, P., Newburgh, L. B., Amiri, M., et al. 2016, ArXiv e-prints, arXiv:1607.01473

Burke-Spolaor, S., Bailes, M., Ekers, R., Macquart, J.-P., & Crawford, III, F. 2011, ApJ, 727, 18

Champion, D. J., Petroff, E., Kramer, M., et al. 2016, MNRAS, arXiv:1511.07746

Chang, T.-C., Pen, U.-L., Bandura, K., & Peterson, J. B. 2010, Nature, 466, 463

Chang, T.-C., Pen, U.-L., Peterson, J. B., & McDonald, P. 2008, Physical Review Letters, 100, 091303

Connor, L., Lin, H.-H., Masui, K., et al. 2016a, MNRAS, 460, 1054

Connor, L., Pen, U.-L., & Oppermann, N. 2016b, MNRAS, 458, L89

Connor, L., Sievers, J., & Pen, U.-L. 2016c, MNRAS, 458, L19

Cordes, J. M., & Wasserman, I. 2016, MNRAS, 457, 232

Danish Khan, M. 2014, ArXiv e-prints, arXiv:1404.5080

Deng, M. 2014, PhD thesis, University of British Columbia,
doi:<http://dx.doi.org/10.14288/1.0167600>

Denman, N., Amiri, M., Bandura, K., et al. 2015, ArXiv e-prints, arXiv:1503.06202

Dodin, I. Y., & Fisch, N. J. 2014, ApJ, 794, 98

Drake, S. 1978, Galileo at work : his scientific biography

Eisenstein, D. J., Zehavi, I., Hogg, D. W., et al. 2005, ApJ, 633, 560

Falcke, H., & Rezzolla, L. 2014, A&A, 562, A137

Faraday, M., & Martin, T. 1936, Faraday's Diary: Nov. 24, 1855-Mar. 12, 1862, Vol. 7
(G. Bell and sons, ltd.)

Furlanetto, S. R., Oh, S. P., & Briggs, F. H. 2006, Phys. Rep., 433, 181

Goldreich, P., & Sridhar, S. 2006, ApJ, 640, L159

Haslam, C. G. T., Salter, C. J., Stoffel, H., & Wilson, W. E. 1982, A&AS, 47, 1

Hewish, A., Bell, S. J., Pilkington, J. D. H., Scott, P. F., & Collins, R. A. 1968, Nature,
217, 709

Jansky, K. G. 1933, Nature, 132, 66

Kashiyama, K., Ioka, K., & Mészáros, P. 2013, ApJ, 776, L39

Katz, J. I. 2014, ApJ, 788, 34

—. 2016, Modern Physics Letters A, 31, 1630013

- Keane, E. F., Stappers, B. W., Kramer, M., & Lyne, A. G. 2012, *MNRAS*, 425, L71
- Keane, E. F., Johnston, S., Bhandari, S., et al. 2016, *Nature*, 530, 453
- Liu, A., & Tegmark, M. 2011, *Phys. Rev. D*, 83, 103006
- Loeb, A., Shvartzvald, Y., & Maoz, D. 2014, *MNRAS*, 439, L46
- Lorimer, D. R., Bailes, M., McLaughlin, M. A., Narkevic, D. J., & Crawford, F. 2007, *Science*, 318, 777
- Lyne, A. G., & Graham-Smith, F. 1998, *Pulsar astronomy*
- Lyutikov, M. 2002, *ApJ*, 580, L65
- Lyutikov, M., Burzawa, L., & Popov, S. B. 2016, *ArXiv e-prints*, arXiv:1603.02891
- Madau, P. 2000, *ArXiv Astrophysics e-prints*, astro-ph/0005106
- Manchester, R. N., & Taylor, J. H. 1977, *Pulsars*
- Maoz, D., Loeb, A., Shvartzvald, Y., et al. 2015, *MNRAS*, 454, 2183
- Masui, K., Lin, H.-H., Sievers, J., et al. 2015, *Nature*, 528, 523
- Morales, M. F., & Wyithe, J. S. B. 2010, *ARA&A*, 48, 127
- Newburgh, L. B., Addison, G. E., Amiri, M., et al. 2014, in *Proc. SPIE*, Vol. 9145, Ground-based and Airborne Telescopes V, 91454V
- Oppermann, N., Connor, L., & Pen, U.-L. 2016, *ArXiv e-prints*, arXiv:1604.03909
- Oppermann, N., Junklewitz, H., Greiner, M., et al. 2015, *A&A*, 575, A118
- Parsons, A., PAPER, & Kilimetre Array South Africa, S. 2014, in *American Astronomical Society Meeting Abstracts*, Vol. 223, American Astronomical Society Meeting Abstracts #223, 404.04

- Parsons, A. R., & Backer, D. C. 2009, *AJ*, 138, 219
- Pen, U.-L., & Connor, L. 2015, *ApJ*, 807, 179
- Pen, U.-L., & Levin, Y. 2014, *MNRAS*, 442, 3338
- Perlmutter, S., Aldering, G., Goldhaber, G., et al. 1999, *ApJ*, 517, 565
- Peterson, J. B., Bandura, K., & Pen, U. L. 2006, *ArXiv Astrophysics e-prints*, astro-ph/0606104
- Petroff, E., Bailes, M., Barr, E. D., et al. 2015a, *MNRAS*, 447, 246
- . 2015b, *MNRAS*, 447, 246
- Petroff, E., Johnston, S., Keane, E. F., et al. 2015c, *MNRAS*, 454, 457
- Petroff, E., Keane, E. F., Barr, E. D., et al. 2015d, *MNRAS*, 451, 3933
- Petroff, E., Barr, E. D., Jameson, A., et al. 2016, *ArXiv e-prints*, arXiv:1601.03547
- Piro, A. L. 2016, *ApJ*, 824, L32
- Popov, S. B., & Postnov, K. A. 2007, *ArXiv e-prints*, arXiv:0710.2006
- Popping, A., & Braun, R. 2008, *A&A*, 479, 903
- Recnik, A., Bandura, K., Denman, N., et al. 2015, *ArXiv e-prints*, arXiv:1503.06189
- Rickett, B. J. 1977, *ARA&A*, 15, 479
- Riess, A. G., Filippenko, A. V., Challis, P., et al. 1998, *AJ*, 116, 1009
- Rybicki, G. B., & Lightman, A. P. 1979, *Radiative processes in astrophysics*
- Scholz, P., Spitler, L. G., Hessels, J. W. T., et al. 2016, *ArXiv e-prints*, arXiv:1603.08880
- Seo, H.-J., & Eisenstein, D. J. 2003, *ApJ*, 598, 720

- Shaw, J. R., Sigurdson, K., Pen, U.-L., Stebbins, A., & Sitwell, M. 2014, *ApJ*, 781, 57
- Shaw, J. R., Sigurdson, K., Sitwell, M., Stebbins, A., & Pen, U.-L. 2015, *Phys. Rev. D*, 91, 083514
- Spitler, L. G., Scholz, P., Hessels, J. W. T., et al. 2016, *Nature*, 531, 202
- Stinebring, D. R., McLaughlin, M. A., Cordes, J. M., et al. 2001, *ApJ*, 549, L97
- Taylor, J. H. 1974, *A&AS*, 15, 367
- Tegmark, M., & Zaldarriaga, M. 2009, *Phys. Rev. D*, 79, 083530
- Thompson, A. R., Moran, J. M., & Swenson, G. W. 1986, *Interferometry and synthesis in radio astronomy*
- Thornton, D., Stappers, B., Bailes, M., et al. 2013, *Science*, 341, 53
- Tingay, S. J., Goetze, R., Bowman, J. D., et al. 2013, *PASA*, 30, e007
- Totani, T. 2013, *PASJ*, 65, L12
- van Haarlem, M. P., Wise, M. W., Gunst, A. W., et al. 2013, *A&A*, 556, A2
- van Leeuwen, J. 2014, in *The Third Hot-wiring the Transient Universe Workshop*, ed. P. R. Wozniak, M. J. Graham, A. A. Mahabal, & R. Seaman, 79–79
- Wang, X., Tegmark, M., Santos, M. G., & Knox, L. 2006, *ApJ*, 650, 529
- Williams, P. K. G., & Berger, E. 2016, *ApJ*, 821, L22
- Zwicky, F. 1933, *Helvetica Physica Acta*, 6, 110